

Wire-EDM machinability investigation on quaternary Ni₄₄Ti₅₀Cu₄Zr₂ shape memory alloy

C. Balasubramaniyan, K. Rajkumar & Santosh S

To cite this article: C. Balasubramaniyan, K. Rajkumar & Santosh S (2021): Wire-EDM machinability investigation on quaternary Ni₄₄Ti₅₀Cu₄Zr₂ shape memory alloy, Materials and Manufacturing Processes, DOI: [10.1080/10426914.2021.1905833](https://doi.org/10.1080/10426914.2021.1905833)

To link to this article: <https://doi.org/10.1080/10426914.2021.1905833>



Published online: 09 Apr 2021.



Submit your article to this journal 



Article views: 29



View related articles 



CrossMark

View Crossmark data 



Wire-EDM machinability investigation on quaternary Ni₄₄Ti₅₀Cu₄Zr₂ shape memory alloy

C. Balasubramaniyan ^a, K. Rajkumar  ^b, and S. Santosh  ^c

^aDepartment of Mechanical Engineering, Sri Venkateswara College of Technology, Chennai, India; ^bDepartment of Mechanical Engineering, Sri Sivasubramaniya Nadar College of Engineering, Chennai, India; ^cDepartment of Metallurgical and Materials Engineering, Indian Institute of Technology-Madras, Chennai, India

ABSTRACT

Shape memory alloy (SMA), also called memory metal, is a smart material that exhibits unique shape memory effect and superelasticity properties. NiTi alloys attract researchers because of their myriad applications in areas such as aerospace, medicine, and robotics. In the present NiTi SMA fabrication, the Cu and Zr elements were added to increase the martensitic transformation temperatures. The current study focuses on the machining of high-temperature Ni₄₄Ti₅₀Cu₄Zr₂ SMA by coated wire electric discharge machining (W-EDM). Machining quality features like surface undulation and material removal were studied by considering current (I), servo voltage (SV), pulse on time (T_{on}), angle of cut (A_C), and pulse off time (T_{off}). Parametric analysis of machining characteristics has been investigated by conducting experiments following the response surface approach based central composite design (RSM-CCD). It was found that MRR has increased by 57% and Ra by 58% with a gradual increase in pulse on time and applied current and decreases gradually on increasing servo voltage and pulse off time. XRD analysis reveals the presence of an oxide layer on the wire-EDMed surface. The study of SEM confirms the formation of the melted layer, micro-voids, and micro-cracks, resulting in surface irregularities.

ARTICLE HISTORY

Received 10 November 2020

Accepted 8 March 2021

KEYWORDS

Spark; erosion; discharge; optimization; roughness; diffraction; oxidation; resolidification

Introduction

Shape memory alloys (SMAs) regain their primary undeformed shape on subjecting them with some stimuli such as heat, magnetic field, etc. This is achieved due to the reversible martensitic transformation occurring in SMAs.^[1] The martensitic transformation temperatures of the SMAs can be altered by varying the Ni/Ti ratio and also by alloying.^[2] NiTi SMAs are widely known owing to their inimitable properties, which include shape memory effect, superelasticity, and corrosion resistance.^[3] In binary NiTi alloys, the functional response of the NiTi SMAs is delayed due to its large thermal hysteresis. This can be surpassed by adding a small percentage of copper and zirconium to reduce the hysteresis.^[4] It is also reported that an increase of more than 4% of copper contributes to two-way transformations.^[5] The transition temperatures depend on the alloying elements and the heat treatment condition.^[1,2] Among the alloying elements, the addition of Cu and Zr to binary NiTi are viable and cost-effective alternatives as they increase the martensitic transformation temperatures and have higher fatigue life.^[6]

A careful and suitable method should be adopted to fabricate these alloys since NiTi in the molten form is highly reactive, which in turn requires a high vacuum to prevent any reactions with oxygen in the atmosphere.^[7] Induction/arc melting in a vacuum chamber, electron/plasma melting are the common methods to fabricate SMAs.^[8,9] Vacuum induction melting is a widely used method to produce NiTi on an industrial scale. In the case of vacuum induction melting

(VIM), graphite crucible is preferred because it can withstand thermal shocks, unlike alumina or magnesia crucibles. Carbon contamination in the melt can be controlled to 200–500 ppm by adopting a special feeding technique of having a Ti-cladding.^[10] Additionally, it is observed that the addition of cobalt in Nickel-Titanium shape memory alloy reduces the martensite initial temperature significantly.^[11]

Machining of SMAs is also a difficult process because of extensive mechanical properties like high toughness, high strength, and high sensitivity to phase transformation temperatures.^[12] Therefore, machining by conventional methods resulted in major changes in the transition temperatures, high heat generation, and high tool wear.^[13] Traditional methods of machining, including drilling, turning, milling and cutting, etc. give rise to many problems such as tool wear, tool breakage, chip burning, etc.^[14,15] Machining SMAs by non-conventional methods leads to fewer surface defects and can produce parts with less surface roughness and intricate shapes.^[16,17] Since NiTi SMAs are widely used in biomedical applications, the final product has highly intricate shapes and contours that are to be machined without much loss in the shape memory properties.^[18] Laser machining of NiTi reported that significant recast layer and ablated layer were formed due to the thermal effects of laser, but defect-free regions with a less recast layer can be obtained with optimal process parameters.^[19] In electrochemical machining, the dissolution of material is very slow and also forms micro pits on the machined surface.^[20] Although water jet machining has no

thermal effects as in laser machining, it leads to many burrs on the machined surface, particularly entrant and exit sides.^[21,22] Wire electric discharge machining (W-EDM) of binary NiTi reported that the material erosion is moderately high as well as showing a nominal surface roughness, compared to other methods.^[23] Spark erosion machining is an advanced non-conventional method which is used to remove the material by the principle of local melting and vaporization. This principle is achieved by producing continuous electrical sparks discharges between the tool wire and the workpiece. This method is mainly used to machine complex shapes by controlling various process parameters.^[15,17] Various research studies on the machining of binary NiTi alloys using W-EDM have been published.^[15–17,24] But the current study mainly focuses on the machining characteristics of quaternary Ni₄₄Ti₅₀Cu₄Zr₂ high temperature shape memory alloy with angular profiles. To achieve high MRR with minimum surface roughness (Ra), the optimal process parameters for machining of Ni₄₄Ti₅₀Cu₄Zr₂ SMA are reported in this research. In this current work, machining experiments were planned based on RSM-CCD with 6 center points using Design expert software 12.0. The application of RSM-CCD optimization technique reduces the cost, time, and effect of noise. ANOVA technique is used to scrutinize the input parameters, which in turn have high control over the MRR and Ra. The machined surface was characterized using SEM and XRD and the presence of recast layer was revealed in some cases.

Materials and methods

Nickel, titanium, copper, and zirconium ingots were purchased in 99.99% pure form from Alfa Aesar, India. Ni₄₄Ti₅₀Cu₄Zr₂ was melted using vacuum induction melting (VIM) using a crucible made of high-density graphite. A layer of Ti-cladding was provided to form a protective TiC layer that prevented any further carbon contamination. A layer of zirconia was coated on a steel mold, which was used to pour the molten alloy to get the required shape. The fabricated SMA was rolled and then homogenized at a temperature of 900°C to achieve the final dimensions. Figure 1 (a) details the fine plates of martensite are seen to coexist in a bed of austenite. Since it is

a high-temperature SMA, martensitic plates are visible in the form of streaks in the room temperature imaging. This feature is a characteristic of a high-temperature SMA, wherein the martensite is not fully transformed at room temperature condition. Upon reaching sufficiently high temperature, it transforms into a fully austenitic structure. Some Ti-rich precipitate particles are also evident in the matrix. These observations are confirmed through the presence of austenite (B2) structure, which is predominant at room temperature, as depicted in figure 1 (b). The fabricated SMA samples were machined using W-EDM (model: YCM- W350). In these experiments, the diameter of the zinc-coated brass wire used for machining was 0.25 mm. Figure 2 shows the W-EDM equipment along with loaded Ni₄₄Ti₅₀Cu₄Zr₂ work material for machining. Figure 3 shows the Ni₄₄Ti₅₀Cu₄Zr₂ machined sample plate with different angular cuts.

The input parameters that were selected for machining of the Ni₄₄Ti₅₀Cu₄Zr₂ SMA along with their range are presented in table 1. The main aim of this experiment is to achieve a high MRR without much compromise on the quality of the machined surface (Ra). A total of 45 experiments were generated by the design expert software according to RSM-CCD. In order to conduct experimentation, some of the machining parameters were kept constant as follows: wire tension of 10 N, a wire feed rate of 2 m/min, and a voltage of open circuit is 80 V.

SMA sample was weighed initially and also after WEDM in a digital weighing balance having a least count of 0.001 mg. The time of machining for each experimental run was recorded. Then material removal rate was estimated by measured weight loss and recorded machining time with density of SMA, as given equation (1),^[25]

$$MRR_7 \text{ (mm}^3/\text{min}) = \frac{W_1 - W_2}{\rho \times t} \times 1000 \quad (1)$$

Where W₁ is the initial weight of the SMA sample before WEDM, W₂ is the final weight of the sample after performing WEDM, the density of work ($\rho = 6.55 \text{ g/cm}^3$), and machining time was noted as 't' in minutes. Surftest SJ-210 instrument was used to evaluate the surface undulation

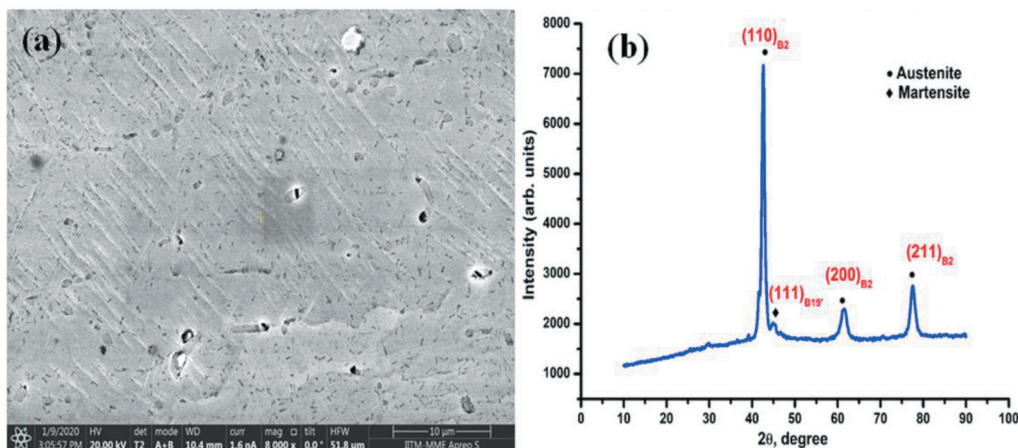


Figure 1. Microstructure and phases of Ni₄₄Ti₅₀Cu₄Zr₂ SMA (a) SEM micrograph (b) XRD.

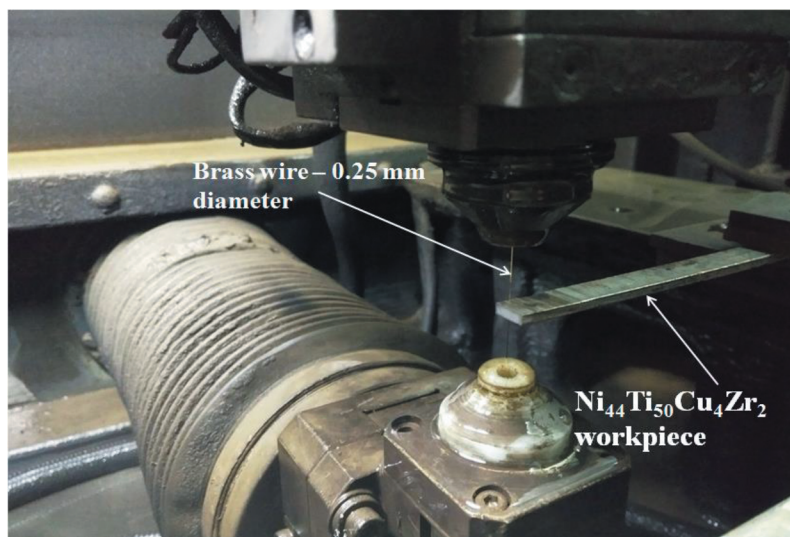


Figure 2. W-EDM setup during machining.

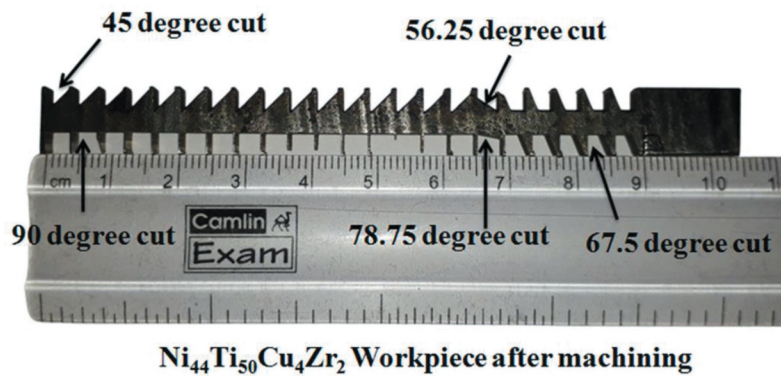


Figure 3. $\text{Ni}_{44}\text{Ti}_{50}\text{Cu}_4\text{Zr}_2$ angular cut after machining.

Table 1. Machining variables and their range.

Input parameters	-2	-1	0	1	2
T_{on} (μs)	8	9	10	11	12
A_C (Degree)	45	56.25	67.5	78.75	90
SV, (V)	40	45	50	55	60
I_s (A)	2	2.75	3.5	4.25	5
T_{off} (μs)	10	11	12	13	14

of the cut surface. Cutoff length of 0.6 mm was considered as a sample length of measurement. The average values of Ra measured in three different areas were reported. Five input parameters were considered for two machining responses and 45 sets of experiments were performed using different combinations. Table 2 presents the measured MRR and Ra for the all set of experiments. These obtained results were given as input to the design expert software for optimization.

Results and discussion

Investigation on MRR and Ra with ANOVA results

The contribution of process variables to the outcomes of machining was determined by the statistical approach of

variance analysis. Further, the optimization results were generated using design expert software. Results observed from ANOVA suggest the adequacy of the quadratic models generated, as verified by a significant test. It has been observed from table 3 that P -value <0.05 illustrates the 95% level of confidence in the established models. These tables show the obtained model F-Value for MRR was 176.32 and the surface roughness was 302.86. These values reveal that the generated models are substantial. Table 3 shows that the most influencing parameter in determining the MRR is the servo voltage with a contribution of 62.52%, and the next is T_{off} with 8.77% and the least influencing parameter is the angle of cut with 0.938%. Table 3 presents the ANOVA for Ra indicating that servo voltage is the most deciding parameter having 66.24% and T_{off} with 9.13%, and the least affecting parameter is the angle of cut with 0.456%. The fit description indicates that the quadratic model is substantial for the study of both Ra and MRR under the response surface methodology. The values of determination coefficient (R^2) for MRR and Ra were 0.9932 and 0.9961 respectively were almost one, suggesting that the performance attributes matched the actual data. The values of R^2 of adjusted & predicted for MRR and Ra were above 90%, indicating a good relationship between process inputs and outcomes. The ideal value of adequate precision, as the

Table 2. MRR and Ra values for different experiments.

Std	Run	T _{on} , μs	T _{off} , μs	SV, V	I, A	A _C , degree	MRR, mm ³ /min	Ra, μm
35	1	10	11	50	3.5	67.5	3.894	2.762
3	2	8	14	40	2	45	3.260	2.288
20	3	12	14	40	2	90	3.555	2.810
5	4	8	10	60	2	45	2.618	1.910
34	5	11	12	50	3.5	67.5	3.932	2.784
16	6	12	14	60	5	45	2.871	2.177
10	7	12	10	40	5	45	4.484	3.730
31	8	8	14	60	5	90	2.473	1.714
14	9	12	10	60	5	45	3.093	2.292
23	10	8	14	60	2	90	1.935	1.579
41	11	10	12	50	3.5	56.25	3.794	2.584
27	12	8	14	40	5	90	3.418	2.331
2	13	12	10	40	2	45	4.345	3.434
1	14	8	10	40	2	45	4.082	2.909
44	15	10	12	50	3.5	67.5	3.802	2.608
17	16	8	10	40	2	90	3.679	2.797
24	17	12	14	60	2	90	2.511	1.801
19	18	8	14	40	2	90	3.158	2.244
4	19	12	14	40	2	45	3.492	2.911
11	20	8	14	40	5	45	3.601	2.390
26	21	12	10	40	5	90	4.327	3.651
29	22	8	10	60	5	90	2.632	1.906
22	23	12	10	60	2	90	2.734	2.009
13	24	8	10	60	5	45	2.751	1.995
39	25	10	12	50	2.75	67.5	3.715	2.443
32	26	12	14	60	5	90	2.881	2.126
21	27	8	10	60	2	90	2.431	1.810
45	28	10	12	50	3.5	67.5	3.768	2.549
40	29	10	12	50	4.25	67.5	3.831	2.693
25	30	8	10	40	5	90	3.708	2.948
9	31	8	10	40	5	45	4.068	3.062
7	32	8	14	60	2	45	2.048	1.667
42	33	10	12	50	3.5	78.75	3.744	2.480
43	34	10	12	50	3.5	67.5	3.780	2.549
30	35	12	10	60	5	90	3.023	2.224
33	36	9	12	50	3.5	67.5	3.665	2.402
18	37	12	10	40	2	90	4.034	3.324
15	38	8	14	60	5	45	2.560	1.758
12	39	12	14	40	5	45	3.802	3.251
36	40	10	13	50	3.5	67.5	3.662	2.464
8	41	12	14	60	2	45	2.581	1.858
37	42	10	12	45	3.5	67.5	3.900	2.897
28	43	12	14	40	5	90	3.727	3.168
38	44	10	12	55	3.5	67.5	3.335	2.309
6	45	12	10	60	2	45	2.875	2.135

prerequisite of a good model, is greater than 4. In the current work, adequate precision with values of 49.2042 and 69.4130 is obtained for MRR and Ra respectively, suggesting a minimum noise effect. The equations (2 & 3) generated mathematically are given below for MRR and Ra.

$$\begin{aligned}
 MRR = & -1.37895 - 0.434979 \times T_{on} - 0.470497 \times T_{off} \\
 & + 0.508629 \times SV - 0.200677 \times I - 0.017678 \times A_C \\
 & + 0.000164 \times T_{off} \times T_{on} + 0.000514 \times SV \times T_{on} \\
 & + 0.000844 \times T_{on} \times I + 0.000558 \times T_{on} \times A_C \\
 & + 0.003777 \times T_{off} \times SV + 0.015677 \times T_{off} \times I \quad (2) \\
 & + 0.000827 \times T_{off} \times A_C + 0.002127 \times SV \times I \\
 & + 0.000104 \times SV \times A_C + 0.000206I \times A_C \\
 & + 0.022987 \times T_{on} + 0.002487 \times T_{off} - 0.006321 \times SV \\
 & - 0.004468 \times I - 0.000051 \times A_C
 \end{aligned}$$

$$\begin{aligned}
 Ra = & +9.45768 + 0.158157 \times T_{on} \\
 & - 0.975126 \times T_{off} - 0.112084 \times SV \\
 & + 0.174698 \times I + 0.055573 \times A_C 38; + 0.005227 \\
 & \times T_{on} \times T_{off} - 0.004730 \times T_{on} \times SV + 0.014969 \times T_{on} \times I \\
 & - 0.000017 \times T_{on} \times A_C + 0.004470 \times T_{off} \times SV + 0.002885 \\
 & \times T_{off} \times I + 0.000188 \times T_{off} \times A_C - 0.000815 \times SV \times I \\
 & + 0.000011 \times SV \times A_C + 0.000140 \times I \times A_C + 0.004207 \\
 & \times T_{on}^2 + 0.024207 \times T_{off}^2 + 0.000568 \times SV^2 - 0.036965 \\
 & \times I^2 - 0.000449A_C^2
 \end{aligned} \quad (3)$$

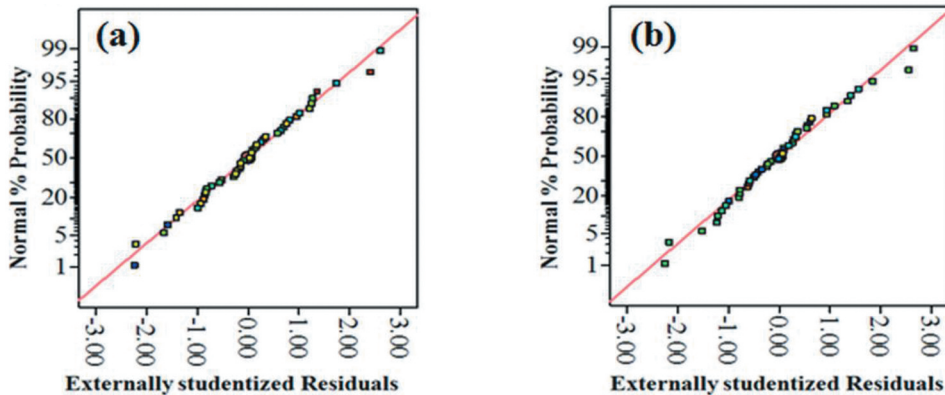
Figure 4 (a, b) shows the normal percentage of probabilities versus externally studentized residuals for MRR and surface roughness. All the points lie in the range, and it signifies that the generated models are very closely fitted to the experimental values since there is no greater deviation, which shows that the design is acceptable.

Process attributes and material removal mechanism

Figure 5 (a-d) represents the MRR of SMA as a function of various machining parameters. **Figure 5** (a) shows that a high T_{on} value of 12 μs and a T_{off} value of 10 μs give a maximum MRR of 4.282 mm³/min. T_{off} regularly produces an intermittent time gap between successive pulses, reducing peak current availability for machining. A long pulse off-time normally increased time duration between effective machining pulses and servo voltage after 45 V tends to slightly increase the working gap between workpiece and electrode were combinedly decrease the MRR.^[26] Therefore, the effect of sparks is limited at high servo voltage leading to poor material removal. **Figure 5** (b) shows that the value of the MRR is strongly influenced by the servo voltage. A high T_{on} value of 12 μs and a servo voltage value of 45 V results in MRR of 4.184 mm³/min. As seen, MRR initially increased and then it started to decrease steadily downward. This is due to an increment of discharge current per spark that increases the MRR. After that, it prevails machining setting conditions for remaining servo voltages. The MRR was reduced to 1.935 mm³/min for the input parameters given at a high servo voltage of 60 V. **Figure 5** (c) indicates that a high T_{on} (12 μs) value and a current of 5 A yields an MRR of 4.174 mm³/min. It is seen that both T_{on} and current were steadily increasing the MRR. An increase in applied current and effective pulse duration increases material removal since more sparks and applied current produce a high amount of melting and vaporization, leading to a greater material removal rate. Ahmari et al.^[27] observed a rise in MRR for NiTi SMA due to the intense sparks that generate melting and vaporization at a high current level. **Figure 5** (d) indicates that the highest material removal of 4.075 mm³/min is seen at a cutting angle of 45° and T_{on} is 12 μs. It is observed that the angle of cut is not much influenced by the MRR. This is an important finding from experimental

Table 3. Statistical ANOVA for MRR and Ra.

Sources	Values of sum square		F-value		p-value		Significant
	MRR	Ra	MRR	Ra	MRR	Ra	
Model	17.65	12.72	176.32	302.86	< 0.0001	< 0.0001	
T _{on}	1.12	1.86	224.69	887.51	< 0.0001	< 0.0001	
T _{off}	1.56	1.19	312.17	565.24	< 0.0001	< 0.0001	
SV	11.11	8.46	2219.93	4027.08	< 0.0001	< 0.0001	
I	0.5271	0.3478	105.29	165.56	< 0.0001	< 0.0001	
A _C	0.167	0.0583	33.37	27.77	< 0.0001	< 0.0001	
T _{on} *T _{off}	0.0001	0.014	0.0028	6.66	0.9586	0.0164	
T _{on} *SV	0.0034	0.2863	0.6756	136.31	0.4192	< 0.0001	
T _{on} *I	0.0002	0.0645	0.041	30.72	0.8413	< 0.0001	
T _{on} *A _C	0.0202	0.0001	4.02	0.0093	0.0562	0.924	
T _{off} *SV	0.1826	0.2558	36.46	121.77	< 0.0001	< 0.0001	
T _{off} *I	0.0708	0.0024	14.14	1.14	0.001	0.296	
T _{off} *A _C	0.0443	0.0023	8.85	1.09	0.0066	0.3063	
SV*I	0.0326	0.0048	6.51	2.27	0.0175	0.1446	
SV*A _C	0.0176	0.0002	3.52	0.0928	0.0728	0.7632	
I*A _C	0.0016	0.0007	0.3104	0.3392	0.5826	0.5657	
T _{on2}	0.0013	0.0002	0.2637	0.0211	0.6123	0.8859	
T _{off2}	0.0001	0.0015	0.0031	0.6969	0.9562	0.4121	
SV2	0.0624	0.0005	12.46	0.24	0.0017	0.6286	
I2	0.0001	0.0011	0.0032	0.5142	0.9557	0.4803	
A _{C2}	0.0001	0.0081	0.0212	3.84	0.8855	0.0619	
Residual	0.1202	0.0504					
Total Corrected mean	17.78	12.77					Not significant
			R ²	0.9932	0.9961		
			Adjusted R ²	0.9876	0.9928		
			Predicted R ²	0.9734	0.9856		
			Adequate Precision	49.2042	69.4130		

**Figure 4.** Probabilities vs externally studentized residuals (a) MRR (b) Ra.

runs. It is inferred that the complex profile and different angles cutting will be done with the same amount of material removal, leading to achieving a planned geometry without considerable error, especially employing quaternary Ni₄₄Ti₅₀Cu₄Zr₂ SMA for bio-implants applications. This is very essential because bio-implants have a complex profile Shukla et al.^[19]

Figure 6(a-b) represents the surface roughness (Ra) of W-EDMed as a function of various machining parameters. It is seen from figure 6 (a) that with a lower T_{on} value of 8 µs and a high T_{off} of 14 µs, a minimum Ra value of 2.246 µm was obtained. Figure 6 (b) indicates a decrease in T_{on} value of 8 µs with a maximum servo voltage value of 60 V resulting in a decrease in Ra of the W-EDMed surface. Besides, a lower Ra of 1.579 µm is seen at a high T_{off} of 14 µs and a high servo voltage of 60 V. It has occurred due to a decrease in the frequency of spark discharges at a higher pulse off time (T_{off}) allowing a lower re-solidification on the machined surface

resulting in a reduction of thermal energy attributed defects, thereby reducing the surface undulation. This figure also shows that the surface roughness value for different cutting angles is almost 2.5 µm.

It is seen from figure 6 (c) that a T_{on} value of 8 µs and a current of 2 A results in a Ra of 2.219 µm. However, the smoothness of the machined surface decreased significantly with an increase of effective pulse duration and applied. Normally, longer pulse duration associated with high current produces stronger and intense spark discharges on the work material. This creates a re-solidified layer, pits, and melted particles of SMA resulting in a poor surface finish. It is also evident that at a high T_{on} value of 12 microseconds and a current of 5 A, high surface roughness of 2.905 µm is observed. This could be due to the generation of more discharge energy that contributes to faster melting and material vaporization, resulting in the formation of micro-cracks and

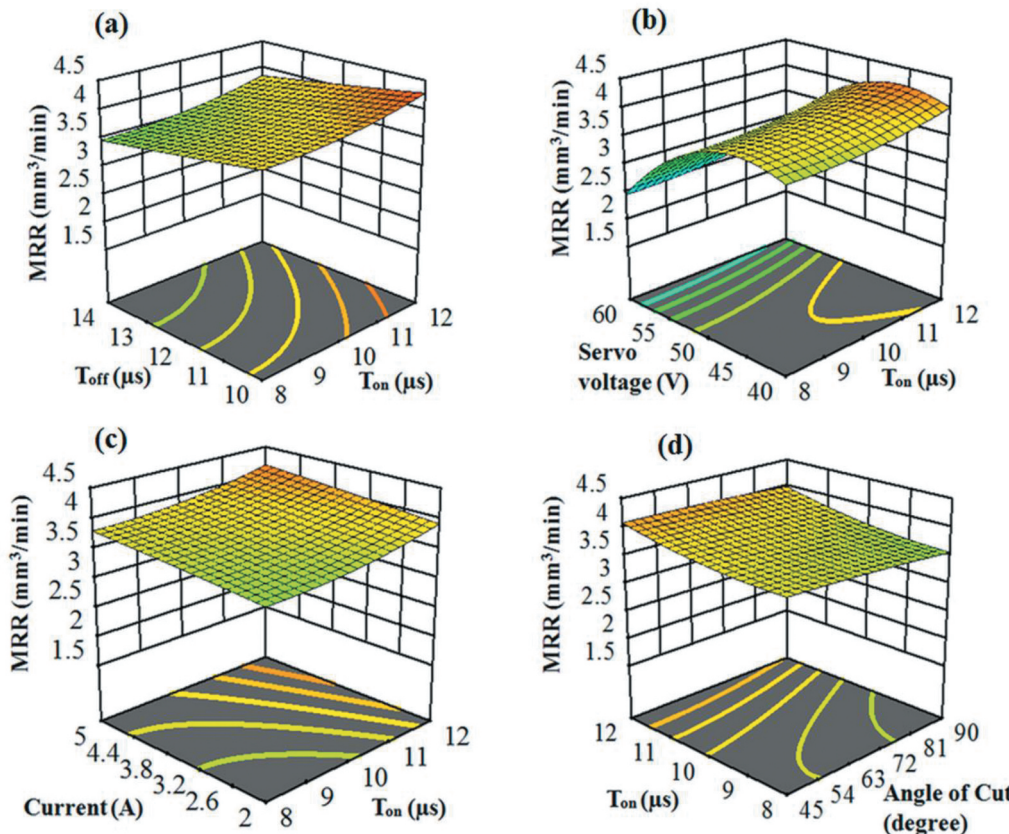


Figure 5. (a-d) 3D response plots for MRR.

craters.^[28] figure 6 (d) depicts an interaction between T_{on} and angle of cut on Ra. An angle of cut of 90° and a T_{on} value of $8 \mu\text{s}$ produce a surface roughness of $2.092 \mu\text{m}$. The surface roughness of machined surface was not much varied from a low to a high angle of cut. It may look like a slight variation but its magnitude is very small.

Multi response optimization of MRR and Ra

Normally, optimum values of input parameters will be used to achieve maximum machining efficiency. In this study, the condition of RSM optimization is to increase MRR and decrease the roughness of the surface. A response surface approach-based desirability analysis was performed to obtain optimal surface roughness and material removal rate and their respective process variables. The optimized parameters for a maximum MRR of $3.6363 \text{ mm}^3/\text{min}$ and minimum Ra of $2.0209 \mu\text{m}$ were found when $T_{on} = 8.00001 \mu\text{s}$, $T_{off} = 13.2752 \mu\text{s}$, SV = 49.1312 V and current = 4.9883 A and angle of cut = 89.999° . The optimized results were also verified experimentally. Upon $T_{on} = 8 \mu\text{s}$, $T_{off} = 13 \mu\text{s}$, SV = 50 V , current (I) = 5 A and angle of cut = 90° , a maximum MRR of $3.781 \text{ mm}^3/\text{min}$ and a minimum Ra of $2.122 \mu\text{m}$ was obtained by experimentation. Figure 7 (a) details the desirability of process attributes and response characteristics that meet the desired requirements of the process. Figure 7 (b) displays the optimized values of the process attributes for desirable outputs from the RSM ramp function.

By evaluating the error results that occur between the experiment and the optimum condition, it can be inferred that the error obtained is very small and can be ignored, as shown in table 4. The machined sample with higher and lower material removal rates of 90° and 45° cuts was chosen for characterization using scanning electron microscopy. The lowest MRR for 90° cut was obtained while machining the sample with the following parameters: $T_{on} = 8 \mu\text{s}$, $T_{off} = 14 \mu\text{s}$, SV = 60 V , I = 2 A , and the highest MRR of 90° cut were obtained while machining with $T_{on} = 12 \mu\text{s}$, SV = 40 V , $T_{off} = 10 \mu\text{s}$, I = 5 A . Therefore, these two samples of 90° cuts were selected for characterization. On the other hand, the highest MRR for 45° cut was obtained when machining with $T_{on} = 12 \mu\text{s}$, $T_{off} = 10 \mu\text{s}$, SV = 40 V , I = 5 A , and minimum MRR was obtained with $T_{on} = 8 \mu\text{s}$, $T_{off} = 14 \mu\text{s}$, SV = 60 V , I = 2 A . These two samples of 45° cut were also considered for characterization to show the trend better.

Surface morphology

Figure 8 (a, b) represents the SEM images of the 45° cut sample with high MRR at high and low magnifications. SEM image of the sample reveals more irregularities such as micro-voids, craters, spherical nodules, protruding particles, many lumps of debris, and molten metal accumulation in large numbers. This can be attributed to the reason that more amounts of material are melted and redeposited on the machined surface at high MRR, causing more irregularities.^[29] Figure 8 (c, d)

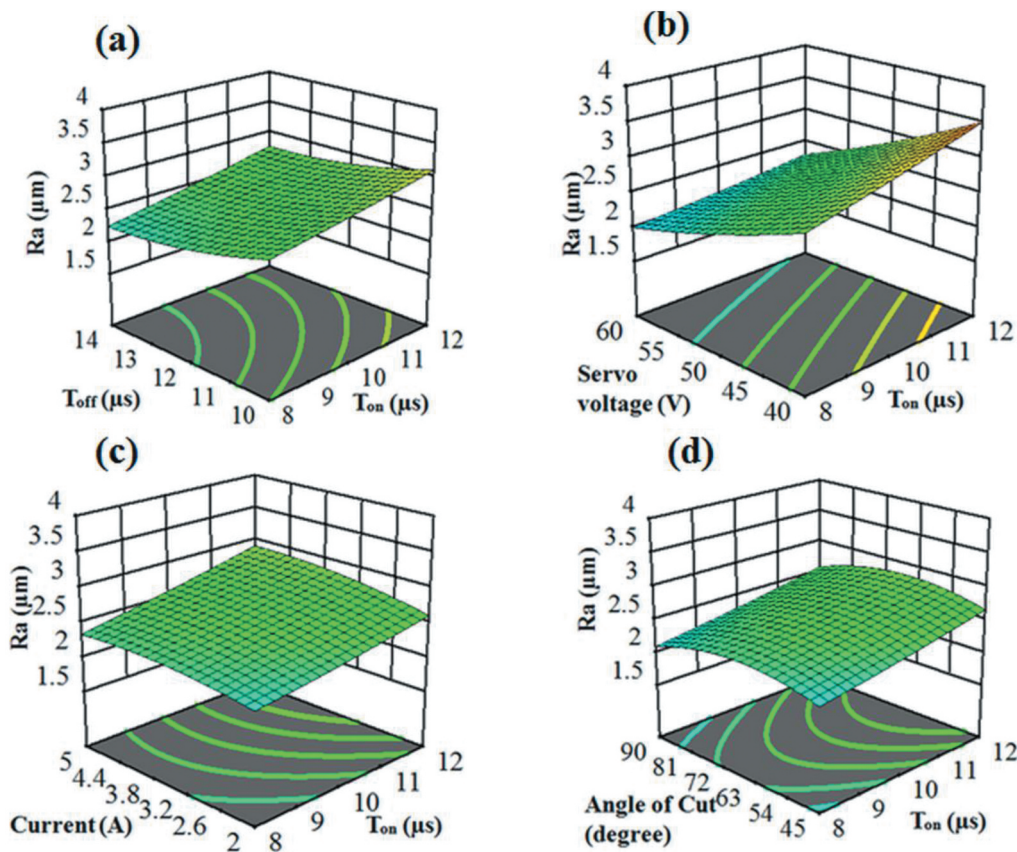


Figure 6. (a-d) 3D response surface plots for R_a .

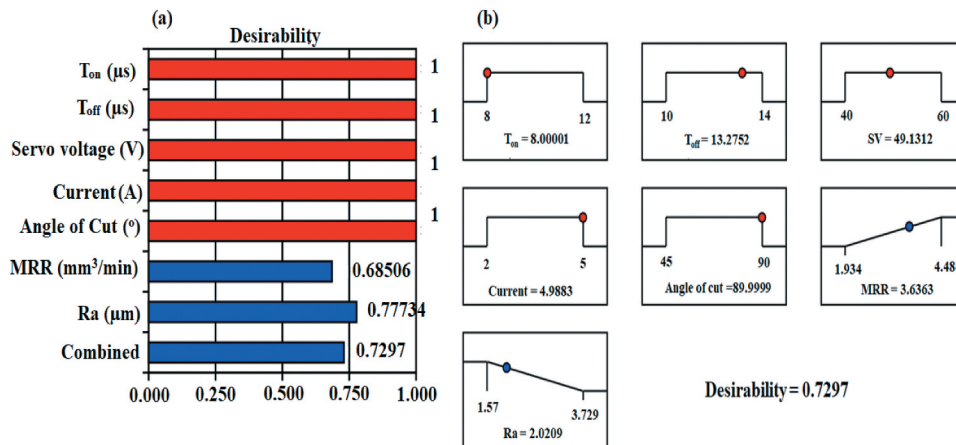


Figure 7. (a) Desirability bar graph (b) Ramp function graph.

Table 4. Predicted and experimental value.

Process parameters at optimized level					RSM Prediction values		Actual experimental values		% of Error	
T_{on}	T_{off}	SV	Current	Angle of Cut	MRR	SR	MRR	SR	MRR	SR
8	13	50	5	90	3.636	2.020	3.781	2.122	3.987	5.049
8	10	50	5	45	3.973	2.285	3.751	2.387	5.587	4.463

represents the SEM images of 45° cut sample machined with low MRR at high and low magnifications. It is evident from the images that the irregularities and defects on this surface are much lesser when compared to that of the samples with high MRR. Some micro-voids and micro-cracks were seen, but an accumulation of debris is very minimal in the case of the

sample with lower MRR than that of high MRR. These defects can also be avoided when optimized parameters are used. Figure 8 (e, f) represents the SEM images of the 90° cut sample with high MRR at high and low magnifications. Analogous to that 45° cut, this sample also showed many surface defects such as micro-voids, cracks, craters, protruding particles,

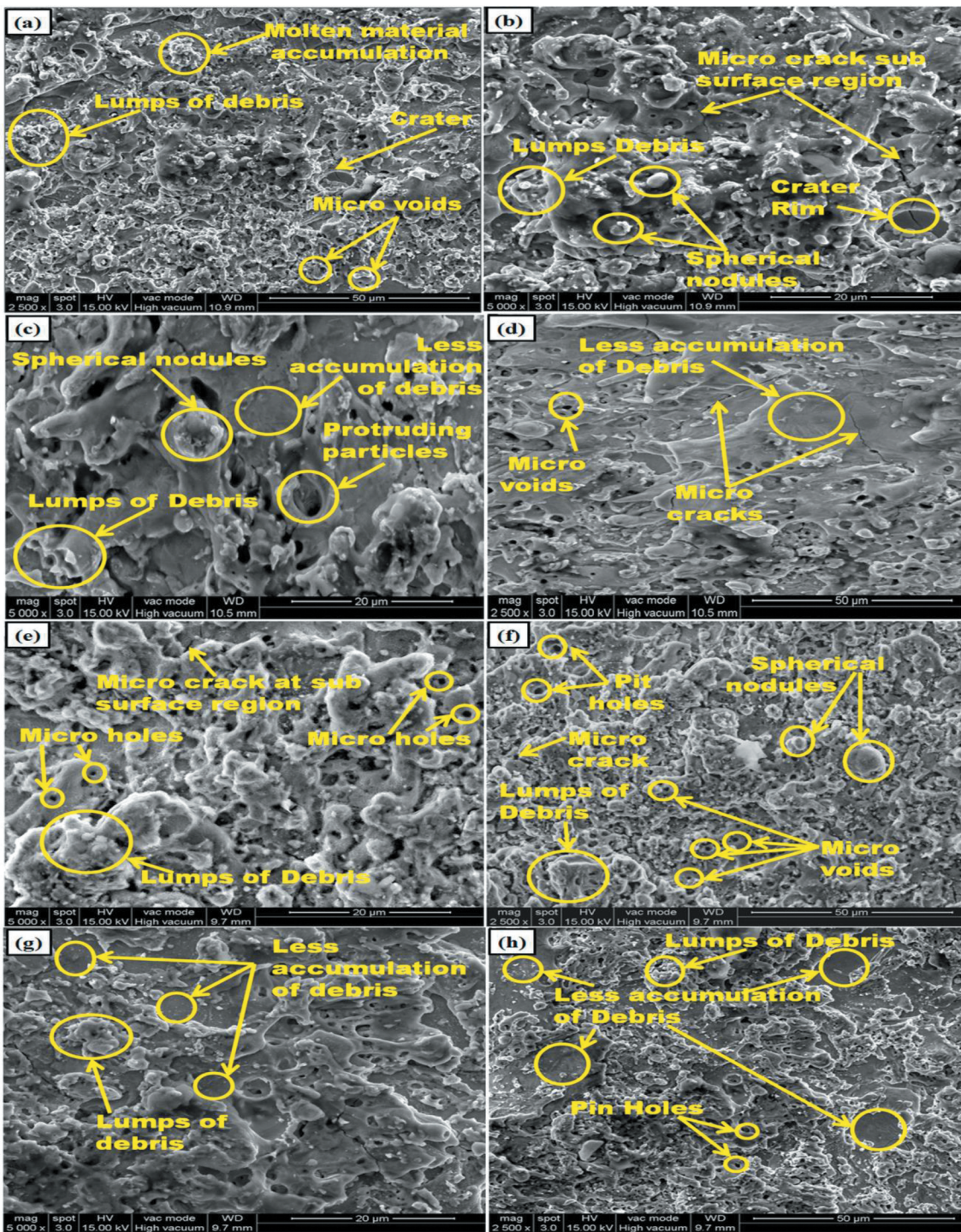


Figure 8. (a-h) Surface morphology of W-EDM machined samples of Ni₄₄Ti₅₀Cu₄Zr₂ alloy after machining.

accumulation of debris, and many pits. Spherical nodules were also observed which is a result of localized melting and deposition. Therefore, in order to achieve higher MRR, surface roughness has to be compromised. Figure 8 (g, h) represents the SEM images of the 90° cut sample with lower MRR at high and low magnifications. The SEM images clearly show that surface defects are considerably reduced. It can be seen that the surface regions in some areas which are proof of less accumulation of debris. However, some micro cracks and pits

were observed. It is evident from the above explanations that samples machined with high MRR, regardless of the angle of cut, had more defects than those with lower MRR conditions, increasing surface undulation.

Figure 9 reveals the X-ray diffractogram of the machined surface. This figure shows the presence of many oxides on the WEDed surface. SEM observation confirms the presence of the recast layer and deposits over the machined surface. The occurrence of oxides such as Cu₂O, ZrO₃, and Ti₂O₃ can be attributed to the reactivity

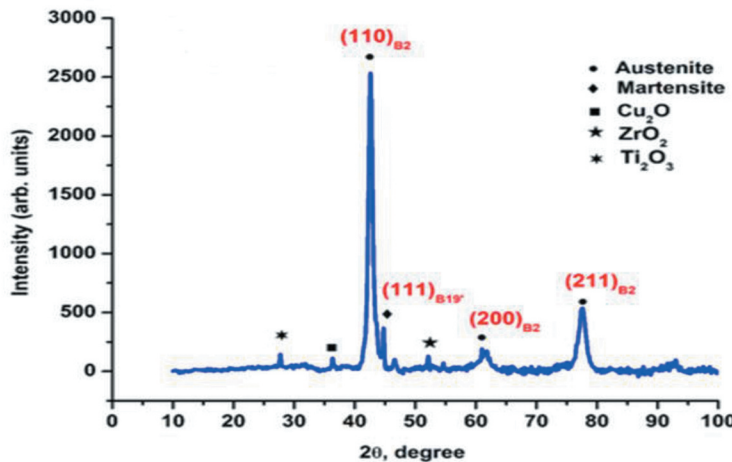


Figure 9. X ray diffractogram of machined $\text{Ni}_{44}\text{Ti}_{50}\text{Cu}_4\text{Zr}_2$ SMA.

of Cu, Zr, and Ti elements that exist in the sample and the brass wire in WEDM. The formation of Cu_2O is because of the deposition of Cu atoms from the brass wire and sample. Likewise, the formation of ZrO_3 and Ti_2O_3 was due to the high activity of Zr and Ti in the sample with a dielectric medium and atmosphere. Similar observations have been made on NiTi SMAs machined with brass wire-EDM.^[3] The development of oxides on the sample has considerably affected the shape recovery property of SMA^[15] when put for any application. Therefore, the formation of oxide layers must be kept minimal to retain the properties of the $\text{Ni}_{44}\text{Ti}_{50}\text{Cu}_4\text{Zr}_2$ SMA.

Conclusions

The study involves the WED machining of $\text{Ni}_{44}\text{Ti}_{50}\text{Cu}_4\text{Zr}_2$ SMA using the RSM-CCD method. The influence of several input parameters like servo voltage, pulse on time, current, and pulse off time has been studied, and their effect on machining characteristics such as surface roughness and material removal rate is reported. Machining characteristics models of those responses were generated for the machining of $\text{Ni}_{44}\text{Ti}_{50}\text{Cu}_4\text{Zr}_2$ SMA. After experimentation and optimization, some of the significant conclusions of this investigation have been drawn and given below,

- (1) Machining of $\text{Ni}_{44}\text{Ti}_{50}\text{Cu}_4\text{Zr}_2$ SMA with high order pulse on duration and applied current increases the MRR as well as surface roughness because more energy was evolved for a longer pulse on duration. This allows the heat generation to increase the local melting and vaporization of the material at a higher rate, resulting in more material removal.
- (2) A low level of surface roughness was recorded at higher servo voltage and pulse off time. It could be due to the combined effect of both variables decreasing discharge energy by increasing the time interval between effective machining pulses as well as increasing the inter-electrode distance. As a result, the surface undulation was reduced to a large extent. Conversely, it reduces

material removal. Angle of cut is one of the process parameters that have little effect on MRR and Ra.

- (3) SEM images of machined $\text{Ni}_{44}\text{Ti}_{50}\text{Cu}_4\text{Zr}_2$ revealed that SMA machined with higher MRR, irrespective of the type of cut, produced more defects like craters, pits, and accumulation of debris than the SMA machined at lower MRR. By machining with higher MRR conditions, the surface roughness will also be high. To obtain smooth cuts for the workpiece, the use of optimum values for the input parameters is essential.
- (4) The highest MRR of $3.781 \text{ mm}^3/\text{min}$ and the lowest Ra of $2.122 \mu\text{m}$ were obtained under optimized parametric conditions of $T_{on} = 8 \mu\text{s}$, $T_{off} = 13 \mu\text{s}$, SV = 50 V, and I = 5 A, and angle of cut = 90° .
- (5) The XRD results confirmed the formation of oxide layers in the $\text{Ni}_{44}\text{Ti}_{50}\text{Cu}_4\text{Zr}_2$ SMA. This can be kept to a minimum by machining with a set of optimized parameters. Wire EDM process is the preferred approach for processing the $\text{Ni}_{44}\text{Ti}_{50}\text{Cu}_4\text{Zr}_2$ Shape memory alloy.

ORCID

- C. Balasubramaniyan <http://orcid.org/0000-0003-3059-7891>
K. Rajkumar <http://orcid.org/0000-0001-6311-3158>
S. Santosh <http://orcid.org/0000-0002-6554-4223>

References

- [1] Mehrpouya, M.; Shahedin, A. M.; Dawood, D. S.; Kamal Ariffin, A. S. An investigation on the optimum machinability of NiTi based shape memory alloy. *Mater. Manuf. Process.* **2017**, *32*(13), 1497–1504. DOI: [10.1080/10426914.2017.1279290](https://doi.org/10.1080/10426914.2017.1279290).
- [2] Pushpanathan, K.; Santhi, R.; Chokkalingam, R. Martensitic transformation, microstructure of Ni-Mn-Ga magnetic shape memory alloy. *Mater. Manuf. Process.* **2012**, *28*(1), 72–78. DOI: [10.1080/10426914.2012.682487](https://doi.org/10.1080/10426914.2012.682487).
- [3] Bisaria, H.; Shandilya, P. Experimental studies on electrical discharge wire cutting of Ni-Rich NiTi shape memory alloy. *Mater. Manuf. Process.* **2018**, *33*(9), 977–985. DOI: [10.1080/10426914.2017.1388518](https://doi.org/10.1080/10426914.2017.1388518).
- [4] Manjaiah, M.; Narendranath, S.; Basavarajappa, S. Wire electro discharge machining performance of TiNiCu shape memory

- alloy. *Silicon*. 2016, 8(3), 467–475. DOI: [10.1007/s12633-014-9273-4](https://doi.org/10.1007/s12633-014-9273-4).
- [5] Velmurugan, C.; Senthilkumar, V. Optimization of spark plasma sintering parameters for NiTiCu shape memory alloys. *Mater. Manuf. Process.* 2019, 34(4), 369–378. DOI: [10.1080/10426914.2018.1512118](https://doi.org/10.1080/10426914.2018.1512118).
- [6] Stroud, H.; Hartl, D. Shape memory alloy torsional actuators: A review of applications, experimental investigations, modeling, and design. *Smart Mater. Struct.* 2020, 29(11), 113001. DOI: [10.1088/1361-665X/abbb12](https://doi.org/10.1088/1361-665X/abbb12).
- [7] Sharma, N.; Jangra, K. K.; Raj, T. Fabrication of NiTi alloy: A review. *Proc. Inst. Mech. Eng. Part L J. Mater. Des. Appl.* 2018, 232(3), 250–269. DOI: [10.1177/1464420715622494](https://doi.org/10.1177/1464420715622494).
- [8] Sadrnezhaad, S. K.; Arami, H.; Keivan, H.; Khalifehzadeh, R. Powder metallurgical fabrication and characterization of nanosstructured porous NiTi shape-memory alloy. *Mater. Manuf. Process.* 2006, 21(8), 727–735. DOI: [10.1080/10426910600727882](https://doi.org/10.1080/10426910600727882).
- [9] Lojen, G.; Stambolić, A.; Šetina Batič, B.; Rudolf, R. Experimental continuous casting of nitinol. *Metals (Basel)*. 2020, 10(4), 505. DOI: [10.3390/met10040505](https://doi.org/10.3390/met10040505).
- [10] Santosh, S.; Sampath, V. Experimental investigations on the effect of copper on the microstructure and shape memory characteristics of NiTi alloys. *IOP Conf. Ser. Mater. Sci. Eng.* 2020, 912(5), 052009. DOI: [10.1088/1757-899X/912/5/052009](https://doi.org/10.1088/1757-899X/912/5/052009).
- [11] Santosh, S.; Sampath, V. Effect of ternary addition of cobalt on shape memory characteristics of Ni-Ti alloys. *Trans. Indian Inst. Met.* 2019, 72(6), 1481–1484. DOI: [10.1007/s12666-019-01604-4](https://doi.org/10.1007/s12666-019-01604-4).
- [12] Liu, J. F.; Li, C.; Fang, X. Y.; Jordon, J. B.; Guo, Y. B. Effect of Wire-EDM on fatigue of nitinol shape memory alloy. *Mater. Manuf. Process.* 2018, 33(16), 1809–1814. DOI: [10.1080/10426914.2018.1512125](https://doi.org/10.1080/10426914.2018.1512125).
- [13] Velmurugan, C.; Senthilkumar, V.; Dinesh, S.; Arulkirubakaran, D. Machining of NiTi-shape memory alloys-a review. *Mach. Sci. Technol.* 2018, 22(3), 355–401. DOI: [10.1080/10910344.2017.1365894](https://doi.org/10.1080/10910344.2017.1365894).
- [14] Bisaria, H.; Shandilya, P. Experimental investigation on wire electric discharge machining (WEDM) of nimonic C-263 superalloy. *Mater. Manuf. Process.* 2019, 34(1), 83–92. DOI: [10.1080/10426914.2018.1532589](https://doi.org/10.1080/10426914.2018.1532589).
- [15] Bisaria, H.; Shandilya, P. Processing of curved profiles on Ni-rich nickel-titanium shape memory alloy by WEDM. *Mater. Manuf. Process.* 2019, 34(12), 1333–1341. DOI: [10.1080/10426914.2019.1594264](https://doi.org/10.1080/10426914.2019.1594264).
- [16] Chaubey, S. K.; Jain, N. K. Investigations on surface quality of WEDM-manufactured meso bevel and helical gears. *Mater. Manuf. Process.* 2018, 33(14), 1568–1577. DOI: [10.1080/10426914.2017.1415440](https://doi.org/10.1080/10426914.2017.1415440).
- [17] Roy, B. K.; Mandal, A. Surface integrity analysis of nitinol-60 shape memory alloy in WEDM. *Mater. Manuf. Process.* 2019, 34(10), 1091–1102. DOI: [10.1080/10426914.2019.1628256](https://doi.org/10.1080/10426914.2019.1628256).
- [18] Leo Kumar, S. P.; Avinash, D. Review on Effect of Ti-alloy processing techniques on surface-integrity for biomedical application. *Mater. Manuf. Process.* 2020, 35(8), 869–892. DOI: [10.1080/10426914.2020.1748195](https://doi.org/10.1080/10426914.2020.1748195).
- [19] Shukla, A. K.; Jayachandran, S.; Bhoyar, J. V.; Akash, K.; Mani Prabu, S. S.; Bhirodkar, S. L.; Manikandan, M.; Shiva, S.; Palani, I. A. Micro-channel fabrication on NiTi shape memory alloy substrate using Nd 3+: YAG Laser. *Mater. Manuf. Process.* 2020, 35(3), 270–278. DOI: [10.1080/10426914.2020.1718703](https://doi.org/10.1080/10426914.2020.1718703).
- [20] Palani, S.; Lakshmanan, P.; Kaliyamurthy, R. Experimental investigations of electrochemical micromachining of nickel aluminum bronze Alloy. *Mater. Manuf. Process.* 2020, 1–10. DOI: [10.1080/10426914.2020.1813888](https://doi.org/10.1080/10426914.2020.1813888).
- [21] Rajesh, M.; Rajkumar, K.; Annamalai, V. E. Abrasive water jet machining on Ti metal-interleaved basalt-flax fiber laminate. *Mater. Manuf. Process.* 2020, 1–12. DOI: [10.1080/10426914.2020.1832692](https://doi.org/10.1080/10426914.2020.1832692).
- [22] Uthayakumar, M.; Khan, M. A.; Kumaran, S. T.; Slota, A.; Zajac, J. Machinability of nickel-based superalloy by abrasive water jet machining. *Mater. Manuf. Process.* 2016, 31(13), 1733–1739. DOI: [10.1080/10426914.2015.1103859](https://doi.org/10.1080/10426914.2015.1103859).
- [23] Chaudhari, R.; Vora, J. J.; Patel, V.; López, D. L.; Parikh, L. N.; Surface, D. M. Analysis of wire-electrical-discharge-machining-processed shape-memory alloys. *Materials (Basel)*. 2020, 13(3), 530. DOI: [10.3390/ma13030530](https://doi.org/10.3390/ma13030530).
- [24] Kang, L.; Yang, C. A. A review on high-strength titanium alloys: Microstructure, strengthening, and properties. *Adv. Eng. Mater.* 2019, 21(8), 1801359. DOI: [10.1002/adem.201801359](https://doi.org/10.1002/adem.201801359).
- [25] Mohanty, A.; Talla, G.; Gangopadhyay, S. Experimental Investigation and Analysis of EDM Characteristics of Inconel 825. *Materials and Manufacturing Processes.* 2014, 29(5), 540–549. DOI: [10.1080/10426914.2014.901536](https://doi.org/10.1080/10426914.2014.901536).
- [26] Soni, H.; M r, M. R. Experimental investigation on effects of wire electro discharge machining of Ti50Ni45Co5 shape memory alloys. *Silicon*. 2018, 10(6), 2483–2490. DOI: [10.1007/s12633-018-9780-9](https://doi.org/10.1007/s12633-018-9780-9).
- [27] Al-Ahmari, A. M. A.; Rasheed, M. S.; Mohammed, M. K.; Saleh, T. A Hybrid machining process combining micro-EDM and laser beam machining of nickel-titanium-based shape memory alloy. *Mater. Manuf. Process.* 2020, 13(3), 447–455. DOI: [10.3390/ma13030530](https://doi.org/10.3390/ma13030530).
- [28] Goyal, A.; Rahman, H., U. R.; Ghani, S. A. C. Experimental investigation & optimisation of wire electrical discharge machining process parameters for Ni49Ti51 shape memory alloy. *J. King Saud Univ. - Eng. Sci.* 2020. DOI: [10.1016/j.jksues.2020.01.003](https://doi.org/10.1016/j.jksues.2020.01.003).
- [29] Chakala, N.; Chandrabose, P. S.; Rao, C. S. Optimisation of WEDM parameters on nitinol alloy using RSM and desirability approach. *Aust. J. Mech. Eng.* 2019, 1–13. DOI: [10.1080/14484846.2019.1681239](https://doi.org/10.1080/14484846.2019.1681239).